PHOTONICS Research

Reflection-type surface lattice resonances in all-metal metasurfaces for refractive index sensing

Liye Li,[1] Yifan Ouyang,[2] Lijun Ma,[1] Hongshun Sun,[1] Yusa Chen,[1] Meizhang Wu,[3,4] Zhimei Qi,[5,6] and Wengang Wu[1,7,8,*]

[1]National Key Laboratory of Science and Technology on Micro/Nano Fabrication, School of Integrated Circuits, Peking University, Beijing 100871, China
[2]School of Electronics, Peking University, Beijing 100871, China
[3]School of Automation, University of Science and Technology Beijing, Beijing 100083, China
[4]School of Instrument Science and Opto-Electronics Engineering, Beijing Information Science and Technology University, Beijing 100096, China
[5]State Key Laboratory of Transducer Technology, Aerospace Information Research Institute, Chinese Academy of Sciences, Beijing 100190, China
[6]University of Chinese Academy of Sciences, Beijing 100049, China
[7]Beijing Advanced Innovation Center for Integrated Circuits, Beijing 100871, China
[8]Frontiers Science Center for Nano-optoelectronics, Peking University, Beijing 100871, China
*Corresponding author: wuwg@pku.edu.cn

Received 1 August 2023; revised 26 September 2023; accepted 15 October 2023; posted 16 October 2023 (Doc. ID 502199); published 30 November 2023

Surface lattice resonance (SLR) is a pretty effective mechanism to realize ultranarrow linewidths in the spectrum. Herein, we propose and demonstrate reflection-type SLRs in all-metal metasurfaces experimentally, compared with the traditional transmission-type SLR, which can avoid the refractive index (RI) mismatch problem and are more suitable for high-efficiency RI sensing due to direct contact and strong light–matter interaction. The measured SLR linewidth is 13.5 nm influenced by the meta-atom size, which needs a compromise design to keep a balance between the narrow linewidth and noise immunity. Notably, the SLR sensitivity is determined by the lattice period along the polarization direction with regularity, which establishes an intuitive link between structures and optical responses and provides a theoretical guide for metasurface designs. Additionally, incident angle multiplexing will make the resonance wavelength red shift or blue shift in the case of orthogonal polarization. The rectangular array metasurface can realize dual SLRs with different sensing performances. Flexibly, the SLR can also be formed by the different meta-atoms and arrays. This research supports SLR multifarious applications involving not only RI sensing but also nonlinear optics, nano-lasers, etc. © 2023 Chinese Laser Press

https://doi.org/10.1364/PRJ.502199

1. INTRODUCTION

The surface plasmon has been regarded as a significant platform recently for achieving refractive index (RI) sensing in biochemical fields [1,2]. The surface plasmon polariton (SPP) sensor is already commercialized but still relies on the prism and cannot analyze the localized RI. The localized surface plasmon resonance (LSPR) on the metal nanoparticles excited by incident beams can compress light into subwavelength volumes to increase the electric field intensity and enhance the light–matter interactions conspicuously [3–6], so that the LSPR response is extremely sensitive to ambient RI changes. Considering other prominent advantages of small size, low weight, and easy integration, the plasmonic metasurface is expected to replace the present ellipsometer and Abbe refractometer to become a new generation of RI sensors. However, the inherent nonradiative Ohmic losses in metal meta-atoms play a terrible role in disturbing sensing performances, resulting in the wider full width at half maximum (FWHM), lower quality factor (Q-factor), small sensitivity, and so on [7–9]. It remains challenging to achieve high-efficiency RI sensing based on traditional plasmonic metasurfaces.

Surface lattice resonance (SLR) in the metasurface is an efficient mechanism to generate narrower resonance FWHMs than those of LSPR by suppressing radiative losses [10–12]. The periodic arrangement of meta-atoms can modulate the incidence to produce one set of diffractive waves parallel to the array plane, that is, the Rayleigh anomaly (RA) wavelength [13,14]. The RA couples with the LSPR to produce the SLR, which belongs to a special Fano resonance essentially [15]. Reshef *et al.* proposed a plasmonic metasurface with an SLR

FWHM of 0.66 nm and a Q-factor of 2340 in the near-infrared band [16]. Yang *et al.* reported an out-of-plane SLR with an FWHM of 0.9 nm at 715 nm in the case of the oblique incidence with transverse magnetic polarization [17]. Nevertheless, the SLR cannot be readily applied in the RI sensing field in most experiments, owing to the low signal-to-noise ratio from the interference of experimental setups and undertested matters. Besides, a number of researches on SLR responses are transmission-type spectra, which require an RI matching layer to maintain RI uniformity in the environment around meta-atoms [18–21]. The RI matching layer in consideration hinders the direct contact between the meta-atom and the matter under test and limits the practicality and efficiency of the sensing.

In this paper, we propose and demonstrate reflection-type SLRs with regularity and flexibility based on all-metal metasurfaces for high-efficiency RI sensing [22]. Because the incident and outgoing beams are in the same RI space all the time, there is no problem with the RI mismatch, which eliminates the need for an additional RI matching layer and couples the matter with the metasurface sufficiently. The size of the meta-atom needs a compromising design due to contradicting requirements on the high signal-to-noise ratio and the ultranarrow FWHM. The lattice period length is a pivotal parameter to control the SLR position in the reflection spectrum and RI sensitivity regularly. On the other hand, the SLR wavelength can be tuned by angle multiplexing to achieve the red shift or blue shift phenomenon under the condition of orthogonal polarization. Furthermore, we can get two SLR spectra with different RI sensitivities in the rectangular array metasurface through polarization multiplexing. In addition, other shaped meta-atoms and array arrangements are also able to realize identical SLR phenomena flexibly. As an outlook, this research promotes the practicability of SLR in the field of RI sensing strongly and provides novel inspirations in nano-lasers [23], nonlinear optics [24], etc.

2. MODELS AND RESULTS

Figure 1(a) exhibits the geometric structure of the proposed metasurface, and the principle of the SLR from the coupling between the LSPR and the RA. The substrate thickness (t_2) is fixed at 150 nm, far larger than the skin depth to prevent transmission light, which will keep the outgoing beam in the same RI space as the incident beam constantly to avoid the RI mismatch. The array is designed as a square arrangement with periods of $P_x = P_y = 500$ nm, and the meta-atom is also square shaped with lengths ($l_x = l_y$) of 250 nm and a thickness (t_1) of 40 nm. Notably, both substrate and meta-atom materials are aluminum, which has high and uniform reflectivity without an interband transition in the whole visible band and can support LSPRs with stability [15,25,26].

In technology, the metasurface sample was fabricated with the following three steps. Step 1: a 150 nm thick Al substrate was sputtered on a clean Si wafer. The vacuum degree of the chamber is around 10^{-6} Torr. Step 2: the e-beam resist (all-resist AR-P 6200.09) was spin-coated on top of the Al substrate at 6000 r/min for 60 s and baked in the hot plate at 150°C for 1 min. Next, the pattern of the meta-atom was conducted by electron beam lithography with 580 pA current and 210 μC/cm^2 doses. The fabricated area is 1 mm × 1 mm. Then, the sample was developed (AR 600-546, 1 min) and fixed (AR 600-60, 30 s). Step 3: we made use of electron beam evaporation to deposit 40 nm thick Al and lift-off based on AR 600-71 solution (over 1 h). We cleaned and dried the sample finally. The corresponding scanning electron microscope (SEM) image is shown in Fig. 1(b). Moreover, the smoothness and height of the meta-atom characterized by the atomic force microscope (AFM) agree well with the design dimensions [Fig. 1(c)].

In principle, the incident wavevector ($\boldsymbol{k}_i$) modulated by the periodic plane array obeys Eq. (1) [27]:

$$n \cdot k_i = |n \cdot \boldsymbol{k}_i \cdot \sin\theta_i + i\boldsymbol{G}_1 + j\boldsymbol{G}_2|, \tag{1}$$

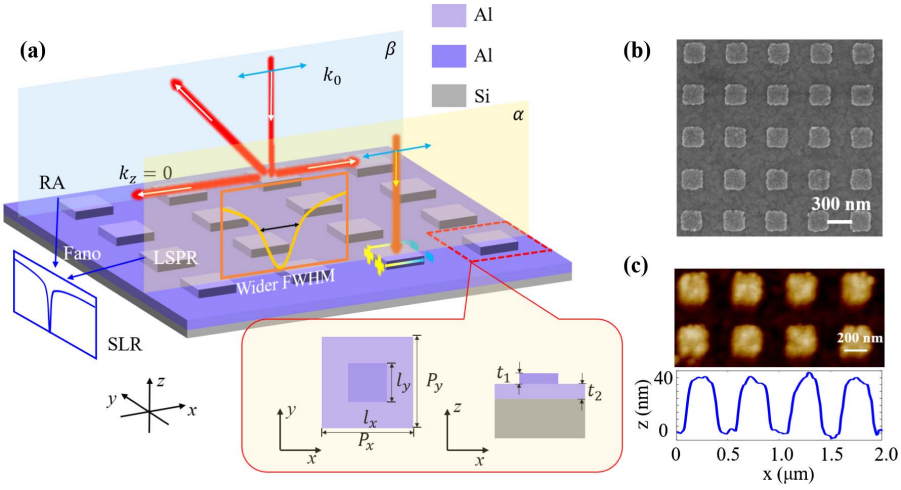

Fig. 1. Schematics and experimental characterization of the proposed all-metal metasurface. (a) Schematic illustration of the all-metal metasurface and the coupling between the LSPR and the RA. The structural parameters are as follows: $P_x = P_y = 500$ nm, $l_x = l_y = 250$ nm, $t_1 = 40$ nm, $t_2 = 150$ nm. (b) SEM image of the fabricated metasurface. (c) Smoothness and height characterizations of the metasurface sample by the AFM.

where n is the environmental RI, θ_i is the incident angle, $\boldsymbol{G}_1$ and $\boldsymbol{G}_2$ represent two-dimensional reciprocal lattice basis vectors of the array, which can be calculated as $|\boldsymbol{G}_1| = |\boldsymbol{G}_2| = 2\pi/P_x$ in the case of the proposed square arrangement, (i, j) are integers defining RA diffraction orders, and the RA wavelength is $\lambda_{\mathrm{RA}} = 2\pi/k_i$. Note that high-order RA waves are existent but cannot couple with LSPRs efficiently, so we only consider the first-order RA, whose (i, j) are defined as $(\pm 1, 0)$ or $(0, \pm 1)$. Hence, Eq. (1) can be simplified in the case of normal incidence in the following form:

$$\lambda_{\mathrm{RA}} = \begin{cases} n \cdot P_x & \text{for } (\pm 1, 0) \text{ order} \\ n \cdot P_y & \text{for } (0, \pm 1) \text{ order} \end{cases}. \tag{2}$$

Obviously, the P_x or P_y is a decisive factor of the λ_{RA} to dominate the SLR property. In the experiment, we attain the SLR spectrum by a macro angular-resolved spectroscopy testing system, composed of a halogen light source (400–1100 nm), a polarizer (extinction ratio, 100:1), a spectrometer, a control system, and so on [28]. The light spot diameter is about 800 μm, because the macro system does not equip an objective. So the number of illuminated unit cells is around 1600 × 1600, which is large enough to overcome the influence of array size [16]. Under the excitation of the normally incident beam with x-polarization, the measured reflection spectrum has a sharp SLR dip at 515.9 nm with an FWHM of 13.5 nm, which is narrower than that of traditional LSPR [Fig. 2(a), blue line] [29–34]. In order to further understand the physics mechanism behind the experimental observations, the numerical simulation is adopted based on the finite-difference time-domain method [35,36]. The simulated SLR position is at 514.7 nm with an absolute error of 1.2 nm [Fig. 2(b), blue line], proving the accuracy of experimental results explicitly. Both resulting SLR wavelengths (λ_{SLR}) are near the λ_{RA} with a little red shift because of the coupling with the LSPR [13]. The electric field E_z distribution on the meta-atom surface at the SLR wavelength shows directionality and periodicity along instead of orthogonal to the polarization [Fig. 2(c)], which demonstrates that the period parallel to the polarization direction determines the RA property, and the SLR belongs to the $(\pm 1, 0)$ order rather than the $(0, \pm 1)$ order. On the other hand, the E_z distribution in the x–z plane is delocalized, not only near the meta-atom but also at the top of the meta-atom [Fig. 2(d)], which can be conducive to strengthening the effective interaction between energy and matter. The influence of meta-atom size on SLR is reflected in the FWHM mainly in that it becomes narrower with the width decreasing, as shown in Figs. 2(a) and 2(b). Although the ultranarrow SLR dip can realize RI sensing with better performances theoretically, it will be submerged in the noise easily attributed to the low noise immunity in the measurement. In essence, the designed 250 nm width is able to balance the ambivalent requirement of high-efficiency RI sensing and high signal-to-noise ratio. Although the metasurface has the potential to support SPP at the metal–air interface, we have demonstrated that the above resonances are from the SLR mechanism instead of the SPP in detail in Appendix A.

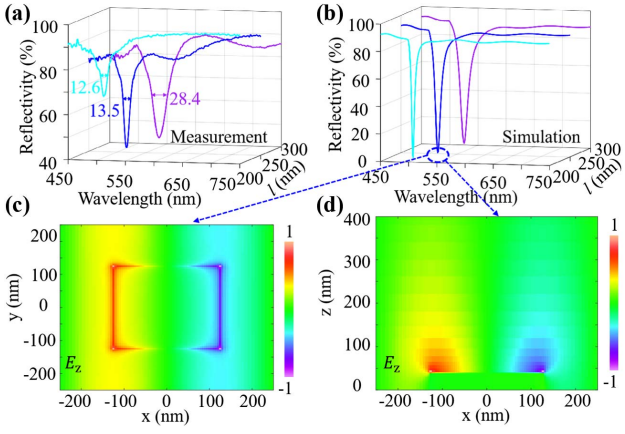

Fig. 2. Experimental and simulated results of the designed metasurface. (a) Measured and (b) numerical simulation reflection spectra of metasurfaces with different meta-atom widths of 200 nm, 250 nm, and 300 nm. Electric field E_z distribution at the SLR wavelength (514.7 nm) in the (c) x–y plane and (d) x–z plane.

As the environmental RI increases, numerical simulation results present that the SLR wavelength will be red shifted with a sensitivity of 518.5 nm/RIU in Figs. 3(a) and 3(b). In the experiment, we only need to immerse the sample in the different liquids (deionized water, anhydrous alcohol, and isopropanol) supported by a groove glass slide, but we need to keep the liquid level flat to avoid additional optical losses. The red shift phenomenon can also be observed [Figs. 3(c) and 3(d)]. The measured sensitivity is 501.8 nm/RIU in great agreement with the simulated one strikingly. The goodness of fit R^2, representing the linearity, can reach 0.9999. Besides, the measured root mean square error (RMSE) value is only 0.1971 nm, meaning that the corresponding RI error is calculated as 3.92×10^{-4} RIU with high accuracy. The depths and FWHMs of SLR dips remain stable, which reflects the perfect noise resistance. The Q-factors are higher generally, and the maximal value can reach 41.6 to achieve longer surface-plasmon dephasing times than traditional LSPRs. The spectral resolution of one spectrometer and sensing sensitivity decide the RI resolution in the system. Hence, when measured by the spectrometer with a 0.1 nm wavelength resolution, the theoretical limit of this metasurface sensor will be 1.99×10^{-4} RIU, which is comparable to the performance of the Abbe refractometer. Also, there are some shallow resonance dips near 500 nm, which are $(\pm 1, \pm 1)$ SLR with lower resonance strengths and RI sensitivities, so we do not care about them.

It is noteworthy that both resulting RI sensitivities from simulation and measurement are near the period length. As a matter of fact, since the SLR wavelength λ_{SLR} is around the λ_{RA}, we can approximate the S_{SLR} based on Eq. (2):

$$S_{\mathrm{SLR}} = \frac{\mathrm{d}\lambda_{\mathrm{SLR}}}{\mathrm{d}n} \approx \frac{\mathrm{d}\lambda_{\mathrm{RA}}}{\mathrm{d}n} = \frac{\mathrm{d}(nP_x)}{\mathrm{d}n} = P_x. \tag{3}$$

Equation (3) establishes a bridge between the geometric configuration and spectrum response creatively and shows the strong regularity, controllability, and simplicity of the SLR in the all-metal metasurface, which offers guidance to actualize an RI sensor with a target sensitivity. Of course, there are a few differences in values between the S_{SLR} and the P_x, resulting from the LSPR interference and manufacturing error.

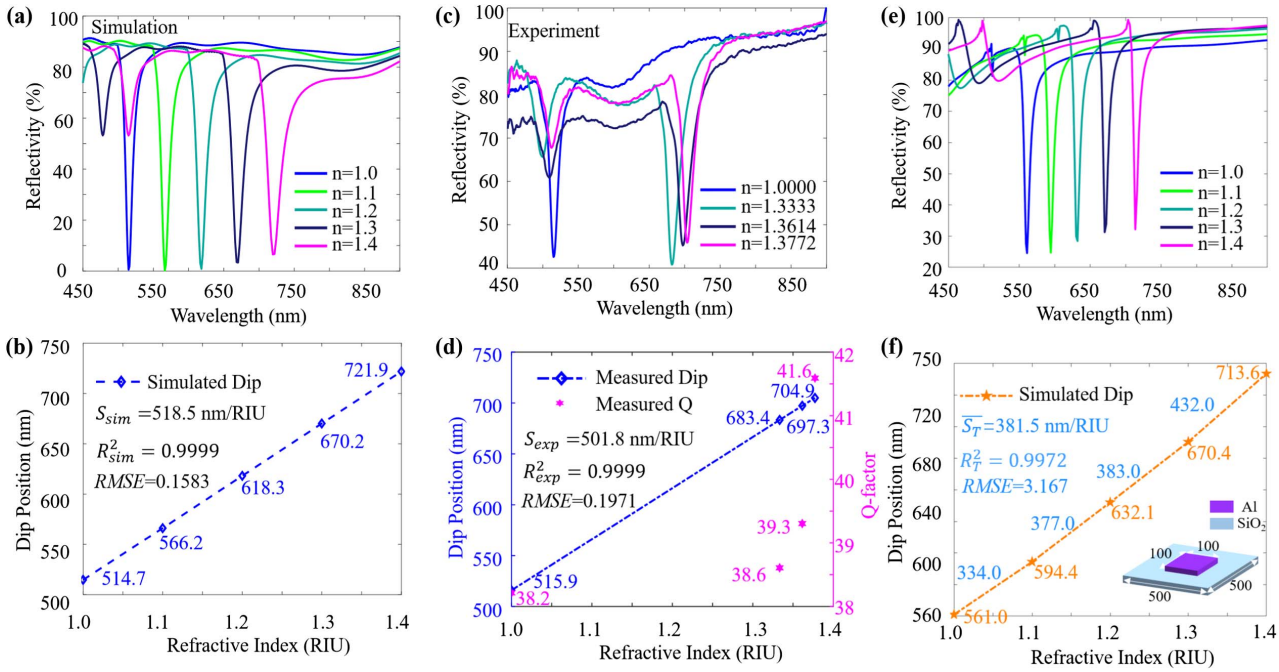

Fig. 3. RI sensing results of numerical simulation and measurement. (a) Variation of simulated SLR spectra with RI environments. (b) SLR dip positions in the spectra and corresponding calculated RI sensing sensitivity. (c) Measured reflection-type SLR spectra under air ($n = 1.0000$), deionized water ($n = 1.3333$), anhydrous alcohol ($n = 1.3614$), and isopropanol ($n = 1.3772$). (d) Measured SLR dip positions, RI sensitivity, and Q-factors. (e) Numerical simulation transmission-type SLR spectra under different RI environments. (f) SLR dip positions and RI sensitivities. The orange line is composed of four line segments with different gradients, with a low linearity. The inset is the designed transmission metasurface model and the length unit is in nanometers.

As for the transmission-type SLR, we establish a three-dimensional metasurface model to analyze and compare the sensitivity based on the numerical simulation [Figs. 3(e) and 3(f)], where the meta-atom is a square nanorod with a width of 100 nm and a height of 40 nm, and the array period sizes are still $P_x = P_y = 500$ nm. Though the transmission-type SLR can also generate a red shift to achieve RI sensing, the sensitivity is not stable, which will decrease from 426.0 nm/RIU to 334.0 nm/RIU gradually with the increase in the difference between environmental RI and the SiO_2 substrate RI. Each simulated sensitivity value is the gradient of a line segment between two SLR points, and four line segments with different gradients lead to a low linearity. The average transmission sensitivity is only 381.5 nm/RIU, with a relative error of over 20% compared with the designed period value. The RI error of 8.3×10^{-3} RIU based on RMSE is one order of magnitude higher than that of the proposed metasurface. In contrast, the reflection-type SLR sensing sensitivity has higher linearity, stability, and regularity.

3. DISCUSSION

The reflection-type SLR mode can be attained flexibly in the whole visible band according to Eq. (2). Keeping other structural parameters invariant, we tune the sizes of the lattice period and meta-atom properly. As shown in Figs. 4(a) and 4(b), the period length of a new all-metal metasurface is defined as 600 nm, matching a square meta-atom with a width of 400 nm. The SLR wavelength in air is 630.59 nm and the RI sensitivity is 618.8 nm/RIU. Similarly, another metasurface with $P_x = 700$ nm and $l_x = 450$ nm generates SLR at 718.07 nm with a sensitivity of 710.5 nm/RIU in the red shift phenomenon [Figs. 4(c) and 4(d)]. The above sensitivity results are all near the designed period values, which provides valid evidence that Eq. (3) is correct and universally applicable in the visible band. (The numerical simulation results about RI sensing are in Appendix B.) With experimental sensitivity values rising, the theoretical RI resolution limit can be improved to 1.62×10^{-4} RIU and 1.41×10^{-4} RIU. As for another two general plasmon materials, Au and Ag, they can also generate SLR phenomena, and corresponding sensitivity values still obey the regularity in Eq. (3) strictly. (The detailed simulated results are shown in Appendix C.)

According to Eq. (1), the incident angle has significant freedom to decide the SLR wavelength. On the one hand, the incident beam with a transverse magnetic (TM) mode excites SLR with the angle θ_i varied from 10° to 50° at a 10° interval. As displayed in Fig. 5(a), the measured SLR wavelengths λ_{SLR}^{TM} in air are red shifted evidently from the visible band to the near-infrared band, following the function nearly in theory:

$$\lambda_{SLR}^{TM} \approx \lambda_{RA}^{TM} = P_x \cdot (n + \sin\theta_i). \tag{4}$$

On the other hand, the SLR from the incident beam with the transverse electric (TE) mode will be blue shifted a little with the angle increasing [Fig. 5(b)], and the SLR linewidth almost keeps invariant. The TE SLR obeys Eq. (5), as follows:

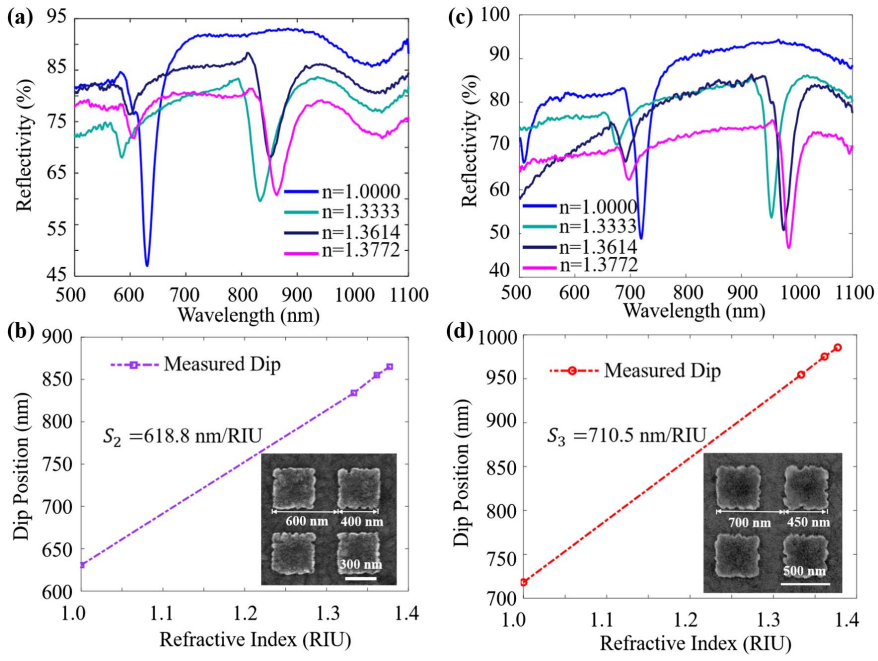

Fig. 4. Spectra and sensitivities of other metasurfaces. (a) Measured reflection-type SLR spectra in different RI environments and (b) RI sensitivity of the metasurface with $P_x = 600$ nm and $l_x = 400$ nm. The inset picture is the SEM image of the sample. Similarly, (c) and (d) are the reflectivity spectra, calculated RI sensitivity, and SEM image of the metasurface with $P_x = 700$ nm and $l_x = 450$ nm.

$$\lambda_{\mathrm{SLR}}^{\mathrm{TE}} \approx \lambda_{\mathrm{RA}}^{\mathrm{TE}} = P_y \cdot \sqrt{n^2 - \sin^2\theta_i}. \tag{5}$$

Also, both resonance positions are mainly determined by the period length parallel to rather than perpendicular to the polarization direction. [Detailed derivation processes of Eqs. (4) and (5) are shown in Appendix D.] In the RI sensing experiment, taking an incident angle of 20° as an example, two SLR modes are sensitive to environmental changes and can achieve the red shift phenomenon with the RI rising [Figs. 5(c) and 5(d)]. The measured sensitivity of TE mode is 497.4 nm/RIU, and the other one is 517.3 nm/RIU. It is worth noting that both sensitivity values are still around the period length. Furthermore, we can approximate the SLR sensitivities $S_{\mathrm{SLR}}^{\mathrm{TM}}$ and $S_{\mathrm{SLR}}^{\mathrm{TE}}$:

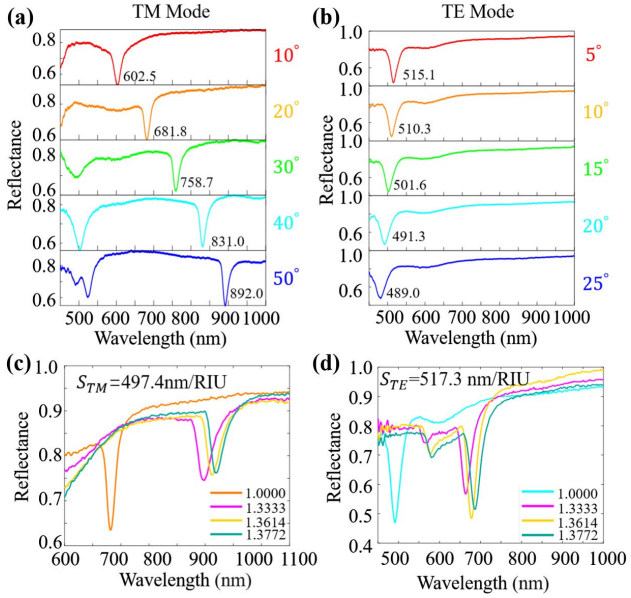

Fig. 5. Experimental results from angular multiplexing with different polarization modes. (a) Measured reflection spectra of the TM beam in the case of different incident angles from 10° to 50° at a 10° interval. (b) Measured reflection spectra of the TE beam with different incident angles from 5° to 25° at a 5° interval. Measured SLR spectra under the different RI conditions of the (c) TM beam and (d) TE beam ($\theta_i = 20°$).

$$S_{\mathrm{SLR}}^{\mathrm{TM}} = \frac{\mathrm{d}\lambda_{\mathrm{SLR}}^{\mathrm{TM}}}{\mathrm{d}n} \approx \frac{\mathrm{d}(P_x \cdot (n + \sin\theta_i))}{\mathrm{d}n} = P_x, \tag{6}$$

$$S_{\mathrm{SLR}}^{\mathrm{TE}} = \frac{\mathrm{d}\lambda_{\mathrm{SLR}}^{\mathrm{TE}}}{\mathrm{d}n} \approx \frac{\mathrm{d}(P_y \cdot \sqrt{n^2 - \sin\theta_i^2})}{\mathrm{d}n} = \frac{n \cdot P_y}{\sqrt{n^2 - \sin\theta_i^2}}$$
$$\approx P_y(\theta_i \to 0°). \tag{7}$$

Obviously, the θ_i will not influence both sensitivities in the case of a small angle range, but the $S_{\mathrm{SLR}}^{\mathrm{TE}}$ is improved efficiently at a larger incident angle, and the maximal value can approach $nP_y/\sqrt{n^2 - 1}$ at $\theta_i = 90°$. The linewidths of TE and TM SLRs are 15.47 nm and 22.21 nm, respectively. Hence, the figures of merit can be calculated as 32.2 and 23.3, larger than those of general LSPR.

Considering that the period along the polarization direction plays a significant part in the reflection-type SLR, we extend the square array to the rectangular array to break the equivalence in the x- and y-directions, which can produce two kinds of SLR responses by polarization multiplexing. Figure 6(a) is an SEM

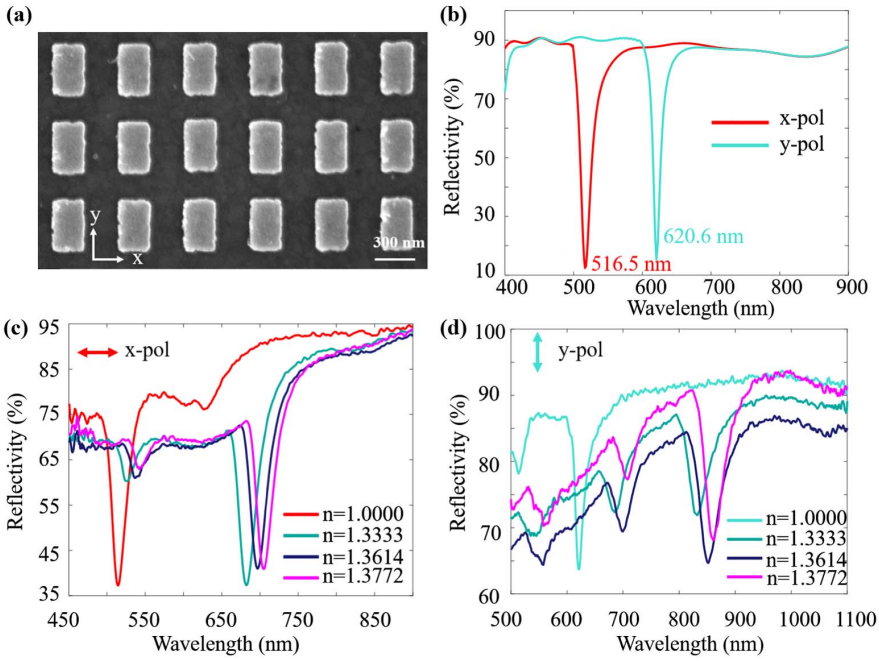

Fig. 6. Experimental results from a rectangular array. (a) SEM image of the all-metal metasurface with the rectangular array ($P_x = 500$ nm, $P_y = 600$ nm) and rectangular meta-atom ($l_x = 250$ nm, $l_y = 400$ nm). (b) Numerical simulation SLR spectra excited by orthogonally polarized incidences. (c), (d) Measured reflection spectra under different RI environments in the case of x- and y-polarizations, separately.

image of a rectangular-array metasurface fabricated by the same process. Compared with the sample in Fig. 1(b), the parameters remain constant in the x-direction, and the period length (P_y) and meta-atom width in the y-direction are tuned as 600 nm and 400 nm, respectively, consistent with the sample in Fig. 4(b). Hence, this metasurface can be seen as a combination of the above two designs and still complies with Eqs. (2) and (3). The resulting spectra from numerical simulation show two different SLRs at 516.5 nm and 620.6 nm excited by orthogonally polarized incidences [Fig. 6(b)]. (Simulation results of electric field distributions are in Appendix E.) In the case of x-polarization, the measured SLR wavelengths will be red shifted with an RI sensitivity of 502.7 nm/RIU [Fig. 6(c)]. However, the spectra and the sensitivity have a few divergences relative to the results in Figs. 3(c) and 3(d), because of the fabrication errors and the crosstalk from measurement errors. On the other hand, the SLR from the y-polarized incident beam belongs to the $(0, \pm 1)$ order. The spectra under different environments are shown in Fig. 6(d), whose sensitivity is 605.0 nm/RIU. Besides, we can also design other combinations of rectangular array periods freely to get two arbitrary sensitivities. (Experimental results of another rectangular array metasurface are shown in Appendix F.)

The same reflection-type SLR effect can be actualized based on other shaped meta-atoms and different array arrangements flexibly. When we change the meta-atom shape from the square to the regular hexagon with a width of 150 nm [Fig. 7(a)], both the measured and simulated SLR wavelengths are hardly affected near 500 nm. As the complementary structure of a nanorod, the nanohole acts as the meta-atom, which can also encourage the LSPR and RA to meet the SLR generation condition [Fig. 7(b)]. And the nanohole metasurface is more advantageous to the enrichment of biological molecules, with application potential in the biosensing field. When the nanohole size is shorter, the SLR intensity will be weaker rather than stronger, following the identical instead of complementary trend to the nanorod. Next, we analyze the influence of the array arrangement on the SLR. The above lattices are the square array or rectangular array that belong to the simplest and the most common design. Furthermore, the hexagonal array and honeycomb array are quite significant as well and exist in some materials, such as the Zn crystal and graphene. We manufacture both arrays as shown in Figs. 7(c) and 7(d), and do not change the meta-atom geometric features. The functions between the RA wavelengths (λ^h_{RA} and λ^c_{RA}) and the lattice constants of a hexagonal or honeycomb array (L^h and L^c) are as follows, respectively:

$$\lambda^h_{\mathrm{RA}} = \frac{\sqrt{3}}{2} \cdot n \cdot L^h, \tag{8}$$

$$\lambda^c_{\mathrm{RA}} = \frac{3}{2} \cdot n \cdot L^c, \tag{9}$$

which are still derived according to Eq. (1) and can also guide the metasurface design. (Detailed derivation processes are in Appendix G.) Since two reciprocal lattice vectors of each plane lattice are identical, the SLR response is polarization independent. For producing RA at the same wavelength (500 nm) as the sample in Fig. 1(b), we define the L^h as 577 nm and the L^c as 333 nm, separately. The experimental and simulated results are as expected. In theory, the RI sensing sensitivity can also be estimated, which is similar to Eq. (3).

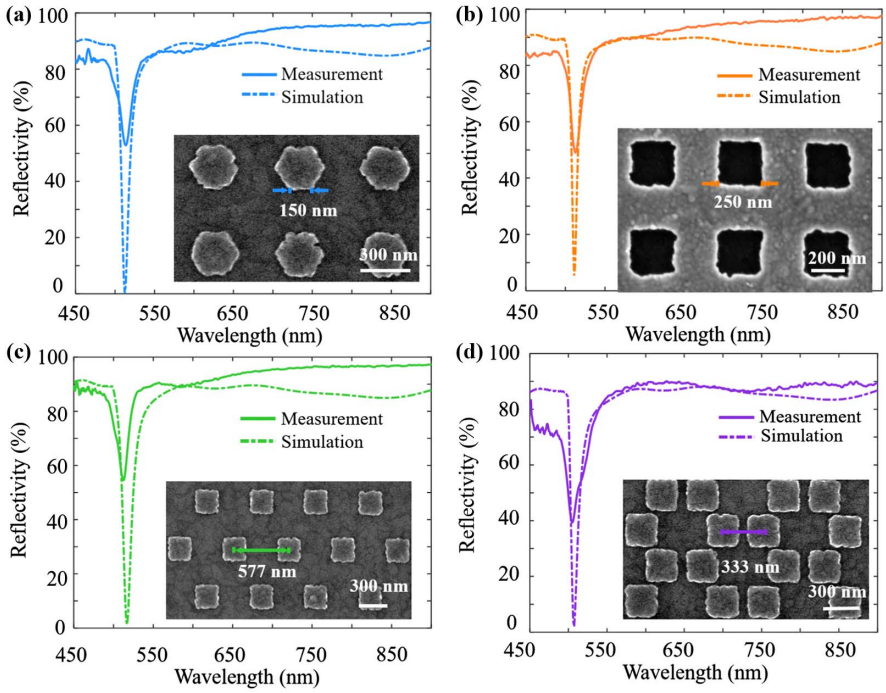

Fig. 7. Measured and simulated spectra and SEM images of metasurfaces with the (a) hexagonal meta-atom, (b) nanohole meta-atom, (c) hexagonal array, and (d) honeycomb array. The above SLR spectra are all excited by *x*-polarized incidence beams.

Compared with other plasmon sensing technologies, the SLR has provided great promise for the development of the next generation of plasmonic integrated sensors with the above prominent advantages. For example, the phase-sensitivity plasmon sensor has a serious angle dependence and requires an ellipsometer to measure the phase shift, which does not satisfy the integration trend [37]. Although the quasi-bound states in the continuum (Q-BIC) theory can generate ultrahigh *Q*-factors, the Q-BIC metasurface has stricter requirements for design and fabrication than those of SLR [38], without a more salient RI sensitivity than SLR and a clear regularity between the sensitivity value and the structural parameter. As for the plasmon waveguide sensor based on the evanescent field, it has a high sensitivity in theory but suffers from propagation losses from material absorption and scattering, which will lead to short optical pathlengths and low interaction strengths in the experiment [39]. The waveguide sensor does not have the angle tunability, polarization multiplexing, or sensitivity regularity of the SLR-based metasurface sensor.

4. CONCLUSION

In conclusion, we have proposed and demonstrated experimentally a reflection-type SLR mode in various all-metal metasurfaces in the visible band for RI sensing with high performances. Compared with the traditional transmission-type SLRs, the all-metal design allows the incident and outgoing light to always be in the same RI space without the requirement of an RI matching layer, which will avoid extra fabricated processes and enhance the light–matter contact and interaction intensely. The period parallel to the polarization direction decides the SLR position in the spectrum and the RI sensing sensitivity based on Eqs. (2) and (3), which establish a link between structures and optical responses and provide a theoretical guide for the metasurface design. Square array metasurfaces with period lengths of 500 nm, 600 nm, and 700 nm can lead to SLRs at 515.9 nm, 630.59 nm, and 718.07 nm, individually, with sensitivities of 501.8 nm/RIU, 618.8 nm/RIU, and 710.5 nm/RIU. The meta-atom width needs to match the period to keep a balance between the narrow FWHM and the high signal-to-noise ratio. The obliquely incident beam with the TM (TE) mode will make SLR wavelength red shift (blue shift) with the angle increasing, whose sensitivities are influenced by the period length still. The rectangular array metasurface engenders two kinds of SLR responses with different RI sensing behaviors, excited by orthogonally polarized beams. The SLR phenomenon is not localized in specific meta-atom structures and array arrangements. When the hexagonal nanorods or nanoholes act as the meta-atom, the same SLR spectra can be formed still. The lattice constants of the hexagonal array and honeycomb array influence the SLR positions and sensitivities likewise. This research proves the regularity, flexibility, and controllability of the SLR enough, which stimulates the development of the SLR mechanism in the nano-laser, nonlinear optics, and RI sensing field in particular.

APPENDIX A: DEMONSTRATION PROCESS OF THE RESONANCE RESPONSE FROM THE SLR MECHANISM INSTEAD OF SPP

In theory, the wavevector k_{SPP} of the first-order SPP is described as follows:

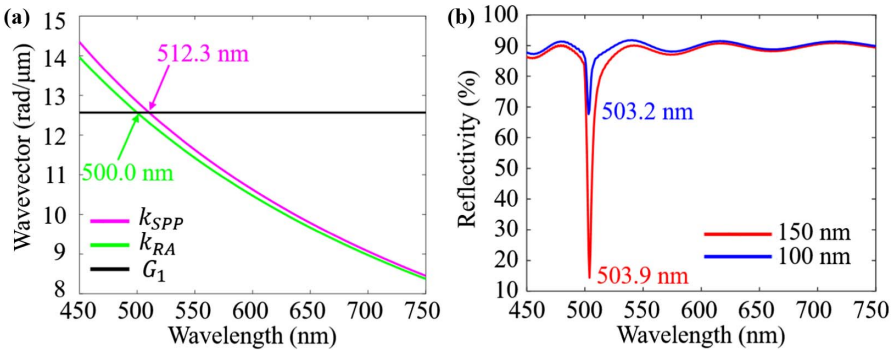

Fig. 8. (a) Theoretical calculation wavelengths of the k_{SPP} and k_{RA}. (b) Simulated spectra of the meta-atoms with widths of 150 nm and 100 nm.

$$k_{SPP} = k_0\sqrt{\frac{\varepsilon_d \cdot \varepsilon_m}{\varepsilon_d + \varepsilon_m}}, \tag{A1}$$

where k_0 is the wavevector in a vacuum. ε_d and ε_m are the relative dielectric constants of the Al metal and the air. The excited wavelength of k_{SPP} needs to match with the reciprocal vector G_1, so that the calculated wavelength λ_{SPP} is 512.3 nm [Fig. 8(a)]. On the other hand, the RA wavelength λ_{RA} is 500 nm according to Eq. (2).

As shown in Figs. 2(a) and 2(b), the larger width of the meta-atom will make the SLR wavelength red shift, so we reduce the width to catch the characteristic of the RA clearly. The simulated spectra of the meta-atoms with widths of 150 nm and 100 nm are displayed in Fig. 8(b). Obviously, both SLR wavelengths (503.9 nm and 503.2 nm) are closer to the λ_{RA} and are far smaller than the λ_{SPP}, which strongly demonstrates that the resonance dip mentioned in the paper is from the SLR mechanism rather than the SPP.

Moreover, we can also prove the conclusion from the view of the resonance depth. Since the strength of LSPR is reduced with the width decreasing, the RA property will be more prominent. The RA cannot localize the light efficiently, so the SLR depth will diminish [Fig. 8(b)]. The above analysis also demonstrates the existence of RA and SLR phenomena.

APPENDIX B: NUMERICAL SIMULATION RESULTS OF METASURFACES WITH $P_x = 600$ nm AND $P_x = 700$ nm FOR RI SENSING

The simulated reflection spectra of the metasurface with $P_x = 600$ nm under different RI environments are shown in Fig. 9(a). The SLR wavelength is red shifted with a sensitivity of 636.2 nm/RIU [Fig. 9(b)], which agrees well with the measured value (618.8 nm/RIU). In addition, as depicted in

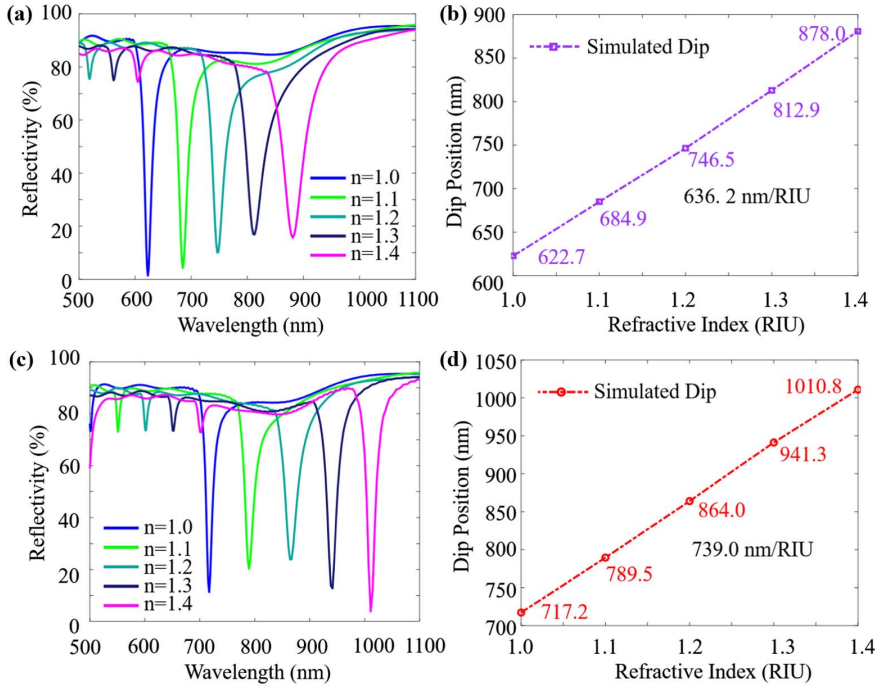

Fig. 9. (a) Simulated reflection spectra and (b) SLR dip positions of the metasurface with $P_x = 600$ nm under different RI environments. (c) Simulated reflection spectra and (d) SLR dip positions of the metasurface with $P_x = 700$ nm under different RI environments.

Figs. 9(c) and 9(d), another metasurface with $P_x = 700$ nm can also generate a red shift phenomenon, whose simulated sensitivity reaches 739.0 nm/RIU. The above-simulated results provide numerical support for the experimental results.

APPENDIX C: SIMULATED SLR RESULTS BASED ON Au AND Ag MATERIALS

Apart from the Al material, Au and Ag are usually used to design plasmon metasurfaces. As shown in Figs. 10(a) and 10(b), a new all-metal metasurface made of Au can support SLR as well, and resonance wavelength is red shifted with the RI increasing. Because Au has an interband transition near 500 nm, we change the period length from 500 nm to 650 nm. The simulated RI sensitivity is 653.0 nm/RIU, which is near the period length obviously and follows Eq. (3) strictly. The Ag-based metasurface is able to excite an SLR response to shift with the environmental RI changes, too [Figs. 10(c) and 10(d)]. The sensitivity (513.3 nm/RIU) is still near the period length (500 nm). Hence, Eq. (3) has universality and applies to the SLR generated by all-metal metasurfaces prepared with Au and Ag materials.

APPENDIX D: DERIVATION OF THE FUNCTION BETWEEN THE INCIDENT ANGLE AND THE SLR WAVELENGTH

In the experiment, the obliquely incident light refracts at the interface between liquid and air before being modulated by a periodic array [Fig. 11(a)], following Snell's law:

$$n_{\text{air}} \cdot \sin\,\theta_i = n \cdot \sin\,\theta_t, \tag{D1}$$

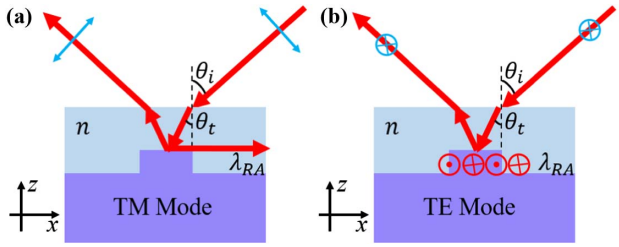

Fig. 11. Schematic diagrams of the (a) TM mode incidence and (b) TE mode incidence.

where n_{air} is the RI of air ($n_{\text{air}} = 1$), θ_i is the incident angle, n is the RI of the liquid under test, and θ_t is the refractive angle that is a little smaller than θ_i, Notably, the θ_t is the actual incidence angle in the liquid environment, and the refraction phenomenon is a non-negligible part in the derivation process.

As for the TM incidence, the projection of polarization on a plane is along the x-direction, so the RA and SLR belong to the x-order. Equation (1) can be simplified in this case:

$$n \cdot \frac{2\pi}{\lambda_{\text{RA}}} = -n \cdot \frac{2\pi}{\lambda_{\text{RA}}} \cdot \sin\,\theta_t + \frac{2\pi}{P_x}. \tag{D2}$$

Considering Eq. (D1), Eq. (D2) can be changed further:

$$n \cdot \frac{2\pi}{\lambda_{\text{RA}}} = -\frac{2\pi}{\lambda_{\text{RA}}} \cdot \sin\,\theta_i + \frac{2\pi}{P_x}. \tag{D3}$$

In fact, Eqs. (D3) and (4) are equivalent.

The TE incidence has a polarization along the y-direction, causing the RA and SLR to be y-order [Fig. 11(b)]. Therefore, we can get the function

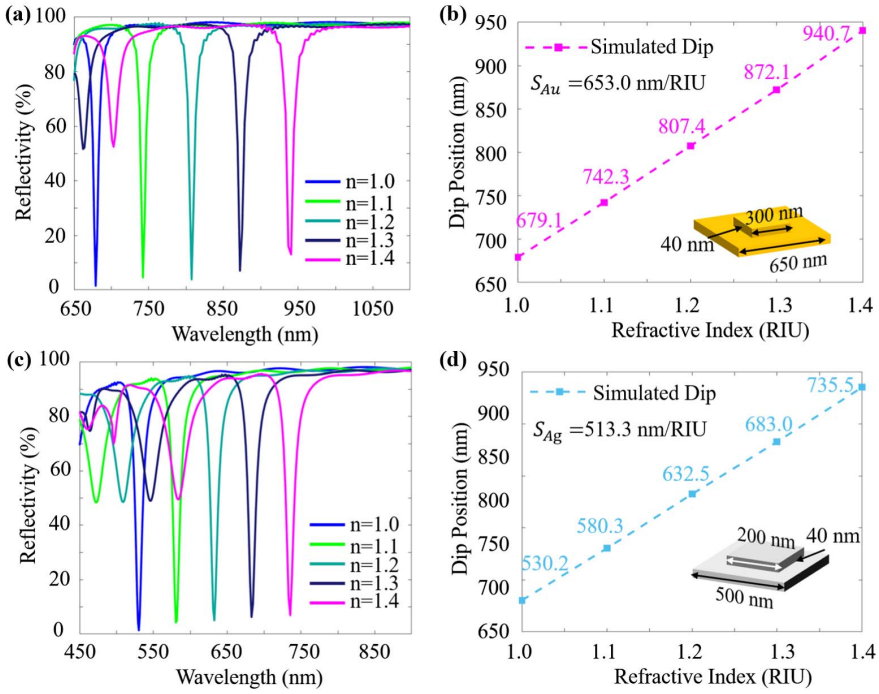

Fig. 10. (a), (b) Simulated reflection spectra and SLR dip positions of the Au metasurface under different RI environments. Inset image is the structure diagram with geometric parameters ($P_x = P_y = 650$ nm, $l_x = l_y = 300$ nm, $t_1 = 40$ nm). (c), (d) Simulated reflection spectra and SLR wavelengths of the Ag metasurface, whose geometric parameters are as follows: $P_x = P_y = 500$ nm, $l_x = l_y = 200$ nm, $t_1 = 40$ nm.

$$n \cdot \frac{2\pi}{\lambda_{RA}} = \left| -n \cdot \frac{2\pi}{\lambda_{RA}} \cdot \sin\theta_t \cdot \vec{x} + \frac{2\pi}{P_y} \cdot \vec{y} \right|, \quad \text{(D4)}$$

where $\vec{x}$ and $\vec{y}$ are the unit vectors in the x- and y-directions, respectively. Similarly, we continue deriving Eq. (D4) based on Eq. (D1):

$$n \cdot \frac{2\pi}{\lambda_{RA}} = \sqrt{\left(\frac{2\pi}{\lambda_{RA}} \cdot \sin\theta_i\right)^2 + \left(\frac{2\pi}{P_y}\right)^2}. \quad \text{(D5)}$$

Furthermore, we simplify Eq. (D5) and get Eq. (5).

APPENDIX E: ELECTRIC FIELD DISTRIBUTIONS AT SLR WAVELENGTHS OF THE RECTANGULAR ARRAY METASURFACE BASED ON NUMERICAL SIMULATION

The SLR at 516.5 nm is from the x-polarized incident beam, and the electric field E_z distribution on the surface of the meta-atom has a distinct periodicity along the polarization direction [Fig. 12(a)]. Similarly, the incidence with y-polarization can excite SLR at 620.6 nm with an electric field distribution parallel to the y-direction [Fig. 12(b)].

APPENDIX F: EXPERIMENTAL RESULTS OF THE RECTANGULAR ARRAY METASURFACE WITH $P_x = 500$ nm AND $P_y = 700$ nm

To further demonstrate the tunability and flexibility of the SLR based on polarization multiplexing, we design another rectangular array metasurface with $P_x = 500$ nm and $P_y = 700$ nm. Corresponding widths are $l_x = 250$ nm and $l_y = 500$ nm. Notably, the meta-atom height is 50 nm instead of 40 nm. Figure 13(a) displays the SEM image of the fabricated metasurface sample. In the case of x-polarization, the SLR is formed at 523.0 nm in air, which will be red shifted with the RI increasing [Fig. 13(b)]. Also, the y-polarized incident beam

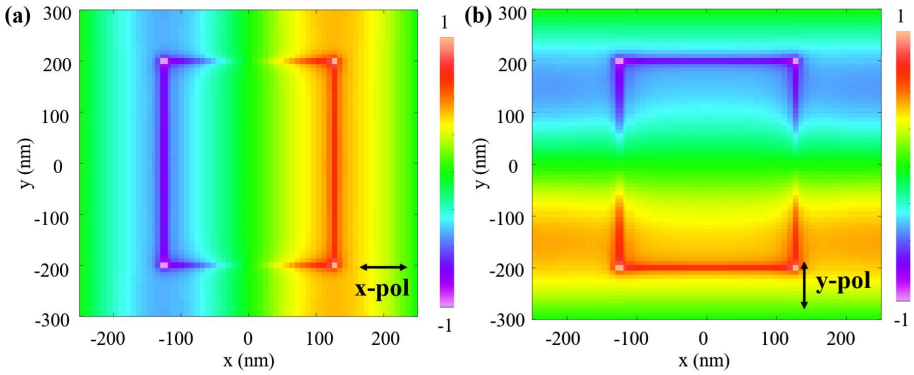

Fig. 12. Normalized electric field E_z distributions on the meta-atom surface in the case of (a) x-polarization and (b) y-polarization.

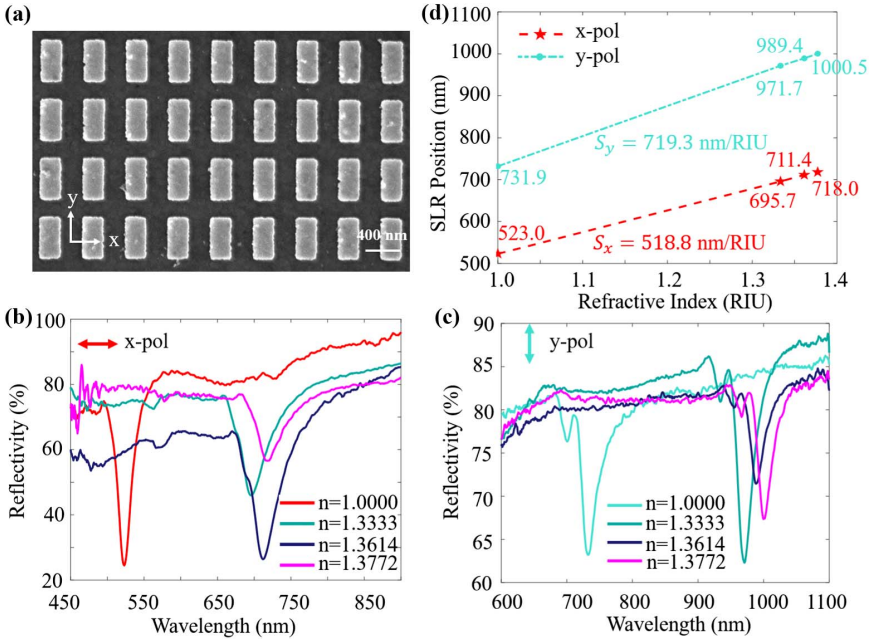

Fig. 13. (a) SEM image of the proposed metasurface with the rectangular array ($P_x = 500$ nm and $P_y = 700$ nm) and rectangular meta-atom ($l_x = 250$ nm, $l_y = 500$ nm, and $h = 50$ nm). (b), (c) Measured reflection spectra under different RI environments in the case of x- and y-polarizations, respectively. (d) SLR positions and corresponding RI sensitivities of both polarization states.

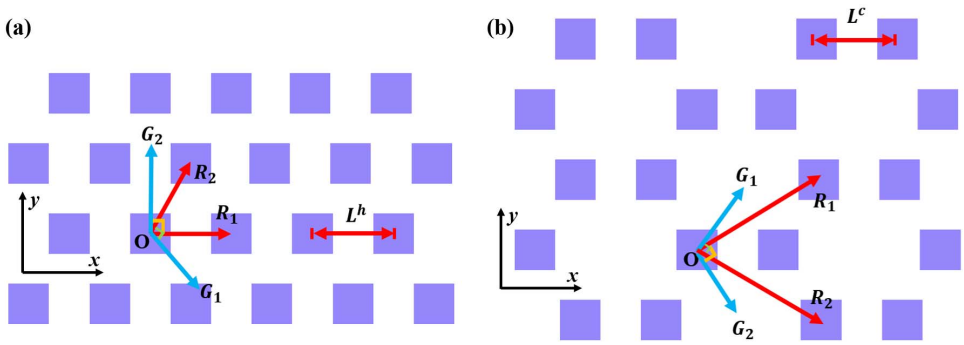

Fig. 14. Schematic diagrams of the (a) hexagonal array and (b) honeycomb array.

generates SLR at 731.9 nm and a red shift phenomenon [Fig. 13(c)]. The sensitivities are 518.8 nm/RIU and 719.3 nm/RIU in Fig. 13(d), separately. Obviously, the above-measured results obey Eq. (2) or Eq. (3) precisely.

APPENDIX G: DERIVATION OF THE FUNCTION BETWEEN THE RA WAVELENGTH AND THE LATTICE CONSTANT IN THE CASE OF THE HEXAGONAL ARRAY AND HONEYCOMB ARRAY

As for the hexagonal array shown in Fig. 14(a), the lattice constant is designed as L^h, and the basis vectors are defined as $\boldsymbol{R}_1 = (L^h, 0)$ and $\boldsymbol{R}_2 = (L^h/2, \sqrt{3}L^h/2)$. $\boldsymbol{G}_1$ and $\boldsymbol{G}_2$ are reciprocal lattice basis vectors, which are calculated as follows:

$$\boldsymbol{G}_p \cdot \boldsymbol{R}_q = 2\pi\delta_{pq} = \begin{cases} 2\pi, & p = q, \\ 0, & p \neq q, \end{cases} \quad p, q = 1, 2. \tag{G1}$$

Hence, we can get $\boldsymbol{G}_1 = (2\pi/L^h, -2\pi/\sqrt{3}L^h)$, $\boldsymbol{G}_2 = (0, 4\pi/\sqrt{3}L^h)$, and $|\boldsymbol{G}_1| = |\boldsymbol{G}_2| = 4\pi/\sqrt{3}L^h$. According to Eq. (1), we can calculate the first-order RA wavelength, taking the $(\pm 1, 0)$ order RA wavelength as an example:

$$n \cdot \frac{2\pi}{\lambda^h_{\mathrm{RA}}} = |\boldsymbol{G}_1| = \frac{4\pi}{\sqrt{3}L^h}. \tag{G2}$$

Finally, we can get the target function as $\lambda^h_{\mathrm{RA}} = \sqrt{3}nL^h/2$.

As for the honeycomb array shown in Fig. 14(b), the lattice constant is L^c, and the basis vectors are defined as $\boldsymbol{R}_1 = (3L^c/2, \sqrt{3L^c}/2)$ and $\boldsymbol{R}_2 = (3L^c/2, -\sqrt{3L^c}/2)$. $\boldsymbol{G}_1$ and $\boldsymbol{G}_2$ are reciprocal lattice basis vectors, which can also be calculated based on Eq. (1). The corresponding results are $\boldsymbol{G}_1 = (2\pi/3L^c, 2\pi/3\sqrt{3}L^c)$, $\boldsymbol{G}_2 = (2\pi/3L^c, -2\pi/\sqrt{3}L^c)$, and $|\boldsymbol{G}_1| = |\boldsymbol{G}_2| = 4\pi/3L^c$. The first-order RA wavelength can be derived as follows:

$$n \cdot \frac{2\pi}{\lambda^c_{\mathrm{RA}}} = |\boldsymbol{G}_1| = \frac{4\pi}{3L^c}. \tag{G3}$$

The final function is $\lambda^c_{\mathrm{RA}} = 3nL^c/2$.

Funding. National Natural Science Foundation of China (61974004, 61931018); National Key Research and Development Program of China (2021YFB3200100).

Acknowledgment. The authors thank Ms. Ling Li and Mr. Jialei Zhu from Ideaoptics Inc. for their help with angular-resolved spectroscopy measurements. The authors thank the Peking Nanofab for providing excellent fabrication conditions.

Disclosures. The authors declare no conflicts of interest.

Data Availability. Data underlying the results presented in this paper are not publicly available at this time but may be obtained from the authors upon reasonable request.

REFERENCES

1. Y. Xu, P. Bai, X. Zhou, Y. Akimov, C. E. Png, L. Ang, W. Knoll, and L. Wu, "Optical refractive index sensors with plasmonic and photonic structures: promising and inconvenient truth," Adv. Opt. Mater. **7**, 1801433 (2019).
2. J. Qin, S. Jiang, Z. Wang, X. Cheng, B. Li, Y. Shi, D. P. Tsai, A. Q. Liu, W. Huang, and W. Zhu, "Metasurface micro/nano-optical sensors: principles and applications," ACS Nano **16**, 11598–11618 (2022).
3. N. Yu and F. Capasso, "Flat optics with designer metasurface," Nat. Mater. **13**, 139–150 (2014).
4. V. G. Kravets, F. Schedin, R. Jalil, L. Britnell, R. V. Gorbachev, D. Ansell, B. Thackray, K. S. Novoselov, A. K. Geim, A. V. Kabashin, and A. N. Grigorenko, "Singular phase nano-optics in plasmonic metamaterials for label-free single-molecule detection," Nat. Mater. **12**, 304–309 (2013).
5. B. Wang, P. Yu, W. Wang, X. Zhang, H. Kuo, H. Xu, and Z. Wang, "High-Q plasmonic resonances: fundamentals and applications," Adv. Opt. Mater. **9**, 2001520 (2021).
6. P. Genevet, F. Capasso, F. Aieta, M. Khorasaninejad, and R. Devlin, "Recent advances in planar optics: from plasmonic to dielectric metasurfaces," Optica **4**, 139–152 (2017).
7. I. M. Pryce, Y. A. Kelaita, K. Aydin, and H. A. Atwater, "Compliant metamaterials for resonantly enhanced infrared absorption spectroscopy and refractive index sensing," ACS Nano **5**, 8167–8174 (2011).
8. J. Hu, S. Bandyopadhyay, Y. Liu, and L. Shao, "A review on metasurface: from principle to smart metadevices," Front. Phys. **8**, 586087 (2021).
9. F. Ding, Y. Yang, R. A. Deshpande, and S. I. Bozhevolnyi, "A review of gap-surface plasmon metasurfaces: fundamentals and applications," Nanophotonics **7**, 1129–1156 (2018).
10. F. Yang, Q. Chen, J. Wang, J. J. Chang, W. Dong, W. Cao, S. Ye, L. Shi, and Z. Nie, "Fabrication of centimeter-scale plasmonic nanoparticle arrays with ultranarrow surface lattice resonances," ACS Nano **17**, 725–734 (2023).
11. V. G. Kravets, A. V. Kabashin, W. L. Barnes, and A. N. Grigorenko, "Plasmonic surface lattice resonances: a review of properties and applications," Chem. Rev. **118**, 5912–5951 (2018).
12. F. Verdelli, J. J. P. M. Schulpen, A. Baldi, and J. G. Rivas, "Chasing vibro-polariton fingerprints in infrared and Raman spectra using

surface lattice resonances on extended metasurfaces," J. Phys. Chem. C **126**, 7143–7151 (2022).
13. P. Offermans, M. C. Schaafsma, S. R. K. Rodriguez, Y. Zhang, M. Crego-Calama, S. H. Brongersma, and J. G. Rivas, "Universal scaling of the figure of merit of plasmonic sensors," ACS Nano **5**, 5151–5157 (2011).
14. H. Gao, J. M. McMahon, M. H. Lee, J. Henzie, S. K. Gray, G. C. Schatz, and T. W. Odom, "Rayleigh anomaly-surface plasmon polariton resonances in palladium and gold subwavelength hole arrays," Opt. Express **17**, 2334–2340 (2009).
15. D. Khlopin, F. Laux, W. P. Wardley, J. Martin, G. A. Wurtz, J. Plain, N. Bonod, A. V. Zayats, W. Dickson, and D. Gérard, "Lattice modes and plasmonic linewidth engineering in gold and aluminum nanoparticle arrays," J. Opt. Soc. Am. B. **34**, 691–700 (2017).
16. M. S. Bin-Alam, O. Reshef, Y. Mamchur, M. Z. Alam, G. Carlow, J. Upham, B. T. Sullivan, J. Ménard, M. J. Huttunen, R. W. Boyd, and K. Dolgaleva, "Ultra-high-Q resonances in plasmonic metasurfaces," Nat. Commun. **12**, 974 (2021).
17. X. Yang, L. Xiong, Y. Lu, and G. Li, "Exceptionally narrow plasmonic surface lattice resonances in gold nanohemisphere array," J. Phys. D **53**, 465109 (2020).
18. A. D. Humphrey and W. L. Barnes, "Plasmonic surface lattice resonances on arrays of different lattice symmetry," Phys. Rev. B **90**, 075404 (2014).
19. A. Yanga, A. J. Hryna, M. R. Bourgeoisb, W. Leea, J. Hua, G. C. Schatzb, and T. W. Odom, "Programmable and reversible plasmon mode engineering," Proc. Natl. Acad. Sci. USA **113**, 14201–14206 (2016).
20. Q. Le-Van, E. Zoethout, E. Geluk, M. Ramezani, M. Berghuis, and J. G. Rivas, "Enhanced quality factors of surface lattice resonances in plasmonic arrays of nanoparticles," Adv. Opt. Mater. **7**, 1801451 (2019).
21. D. Wang, A. Yang, A. J. Hryn, G. C. Schatz, and T. W. Odom, "Superlattice plasmons in hierarchical au nanoparticle arrays," ACS Photon. **2**, 1789–1794 (2015).
22. Z. Li, S. Butun, and K. Aidin, "Ultranarrow band absorbers based on surface lattice resonances in nanostructured metal surfaces," ACS Nano **8**, 8242–8248 (2014).
23. A. Yang, T. B. Hoang, M. Dridi, C. Deeb, M. H. Mikkelsen, G. C. Schatz, and T. W. Odom, "Real-time tunable lasing from plasmonic nanocavity arrays," Nat. Commun. **6**, 6939 2015.
24. R. Czaplicki, A. Kiviniemi, J. Laukkanen, J. Lehtolahti, M. Kuittinen, and M. Kauranen, "Surface lattice resonances in second-harmonic generation from metasurfaces," Opt. Lett. **41**, 2684–2687 (2016).
25. M. Miyata, H. Hatada, and J. Takahara, "Full-color subwavelength printing with gap-plasmonic optical antennas," Nano Lett. **16**, 3166–3172 (2016).
26. Z. Li, W. Wang, D. Rosenmann, D. A. Czaplewski, X. Yang, and J. Gao, "All-metal structural color printing based on aluminum plasmonic metasurfaces," Opt. Express **24**, 20472–20480 (2016).
27. Y. Shen, J. Zhou, T. Liu, Y. Tao, R. Jiang, M. Liu, G. Xiao, J. Zhu, Z. Zhou, X. Wang, C. Jin, and J. Wang, "Plasmonic gold mushroom arrays with refractive index sensing figures of merit approaching the theoretical limit," Nat. Commun. **4**, 2381 (2013).
28. http://www.ideaoptics.com/.
29. J. Yao, A. P. Le, S. K. Gray, J. S. Moore, J. A. Rogers, and R. G. Nuzzo, "Functional nanostructured plasmonic materials," Adv. Mater. **22**, 1102–1110 (2010).
30. Q. T. Trinh, S. K. Nguyen, D. H. Nguyen, G. K. Tran, V. H. Le, H. S. Nguyen, and Q. L. Van, "Coexistence of surface lattice resonances and bound states in the continuum in a plasmonic lattice," Opt. Lett. **47**, 1510–1513 (2022).
31. V. E. Babicheva and A. B. Evlyukhin, "Resonant lattice Kerker effect in metasurfaces with electric and magnetic optical responses," Laser Photon. Rev. **11**, 1700132 (2017).
32. C. Cherqui, M. R. Bourgeois, D. Wang, and G. C. Schatz, "Plasmonic surface lattice resonances: theory and computation," Acc. Chem. Res. **52**, 2548–2558 (2019).
33. B. R. Lu, C. Xu, J. Liao, J. Liu, and Y. Chen, "High-resolution plasmonic structural colors from nanohole arrays with bottom metal disks," Opt. Lett. **41**, 1400–1403 (2016).
34. Y. Chu, E. Schonbrun, T. Yang, and K. B. Crozier, "Experimental observation of narrow surface plasmon resonances in gold nanoparticle arrays," Appl. Phys. Lett. **93**, 181108 (2008).
35. T. Aoudjit, A. Horrer, S. Kostcheev, R. Bachelot, J. Plain, and D. Gérard, "Photochemical imaging of near-field and dissymmetry factor in chiral nanostructures," Adv. Opt. Mater. **11**, 2203015 (2023).
36. J. Wang, J. Zheng, K. H. Li, J. Wang, H. Q. Lin, and L. Shao, "Excitation of chiral cavity plasmon resonances in film-coupled chiral Au nanoparticles," Adv. Opt. Mater. **11**, 2202865 (2023).
37. V. G. Kravets, F. Schedin, A. V. Kabashin, and A. N. Grigorenko, "Sensitivity of collective plasmon modes of gold nanoresonators to local environment," Opt. Lett. **35**, 956–958 (2010).
38. H. H. Hsiao, Y. C. Hsu, A. Y. Liu, J. C. Hsieh, and Y. H. Lin, "Ultrasensitive refractive index sensing based on the quasi-bound states in the continuum of all-dielectric metasurfaces," Adv. Opt. Mater. **10**, 2200812 (2022).
39. M. Vlk, A. Datta, S. Alberti, H. D. Yallew, V. Mittal, G. S. Murugan, and J. Jágerská, "Extraordinary vanescent field confinement waveguide sensor for mid-infrared trace gas spectroscopy," Light Sci. Appl. **10**, 26 (2021).